Chin. J. Astron. Astrophys. Vol. 8 (2008), No. 2, 133–145
(*http://www.chjaa.org*)

Chinese Journal of
Astronomy and
Astrophysics

Determination of the Topology Skeleton of Magnetic Fields in a Solar Active Region *

Hui Zhao[1], Jing-Xiu Wang[1], Jun Zhang[1], Chi-Jie Xiao[1] and Hai-Min Wang[2]

[1] National Astronomical Observatories, Chinese Academy of Sciences, Beijing 100012;
wangjx@bao.ac.cn
[2] Big Bear Solar Observatory, 40386 North Shore Lane, Big Bear City, CA 92314, USA

Received 2007 September 20; accepted 2007 September 30

Abstract Magnetic topology has been a key to the understanding of magnetic energy release mechanism. Based on observed vector magnetograms, we have determined the three-dimensional (3D) topology skeleton of the magnetic fields in the active region NOAA 10720. The skeleton consists of six 3D magnetic nulls and a network of corresponding spines, fans, and null-null lines. For the first time, we have identified a spiral magnetic null in Sun's corona. The magnetic lines of force twisted around the spine of the null, forming a 'magnetic wreath' with excess of free magnetic energy and resembling observed brightening structures at extra-ultraviolet (EUV) wavebands. We found clear evidence of topology eruptions which are referred to as catastrophic changes of topology skeleton associated with a coronal mass ejection (CME) and an explosive X-ray flare. These results shed new lights on the structural complexity and its role in explosive magnetic activity. The concept of flux rope has been widely used in modelling explosive magnetic activity, although their observational identity is rather obscure or, at least, lacking of necessary details up to date. We suggest that the magnetic wreath associated with the 3D spiral null is likely an important class of the physical entity of flux ropes.

Key words: Sun: magnetic fields — Sun: solar corona — Sun: activity

1 INTRODUCTION

The self-closure and frozen-in condition of magnetic fields in astrophysical and space plasmas make the electromagnetic interaction extremely complicated in the sense that the magnetized plasma is divided into distinct topologies. Explosive release of stored magnetic energy, which appears presumably in the topology interface, can not be realized without topology collapse. Now, solar active regions (ARs) represent a typical example of electromagnetic interaction. They are characterized by strong magnetic fields with complex topology, serving as a paradigm in astrophysics and space science. Since late 1940s it has been recognized that under certain conditions a breakdown of magnetic topology could produce solar flares and cosmic ray particles (Giowanelli 1946; Sweet 1958). It is fundamental for the understanding of explosive solar activity to explore the magnetic skeleton in the AR which is composed of magnetic nulls (neutral points) and a network of spines (γ lines) and fans (Σ surfaces) (Lau & Finn 1990; Parnell et al. 1996; Priest et al. 1997). This, in turn, will guide us to a thorough understanding of the ubiquitous magnetic activity in the universe.

The 3D topology skeleton of Sun's magnetic fields, composed of nulls, spines, fans and separators (Priest et al. 1997), has only been described either by simple analytical models (Lau 1993; Brown & Priest 2001; Parnell 2007), or by theoretical calculations with 'magnetic charges' or 'dipoles' to approximate

* Supported by the National Natural Science Foundation of China.

the observed magnetic fields on the solar surface (Seehafer 1986; Gorbachev & Somov 1988; Démoulin et al. 1992; Longcope & Klapper 2002; Longcope 2005). By comparing the brightness observations with the above conceptual models, Filippov (1999), Aulanier et al. (2000), Fletcher et al. (2001), Maia et al. (2003) and Li et al. (2006) identified 3D nulls in the corona. These approaches have demonstrated that there, indeed, exist 3D magnetic nulls with spines and fans in the corona, forming a skeleton of magnetic topology. In addition, the magnetic energy release in solar flares is closely associated with these topological structures. However, as too many simplifications are involved, e.g., the representation of the observed fields by discrete 'magnetic charges' or 'dipoles' and the assumption of current-free (potential) fields, we are far from being able to evaluate current status of our knowledge about the real magnetic skeleton, let alone the nature of 3D magnetic reconnection in the solar atmosphere (Parnell 2007). It is only recently that 3D magnetic nulls are identified in the geomagnetic tail based on the *in situ* measurements with Spacecraft Cluster (Xiao et al. 2006). On the other hand, separatrices can also be approached by discontinuities in the footpoint mapping that is defined in a continuous magnetic boundary (Low 1987; Low & Wolfson 1988). These discontinuities ascribe coronal nulls or bald patches (Seehafer 1986; Titov et al. 1993; Bungey et al. 1996). Some authors (Priest & Démoulin 1995; Démoulin et al. 1996; Titov et al. 2002) have given measurements of mapping distortion or squashing to accurately locate the so-called quasi-separatrix layer (QSL). The QSL method is not a direct way to determine the separatrices, and it would take more time than the magnetic charge topology (MCT) method (Longcope 2005) to approach the same singular feature. Nor can we obtain a clear skeleton from a footpoint mapping of the magnetic boundary, as it departs from the nulls. However, to study the features in the photosphere or lower corona, it is still a useful tool because of its precise measurement of the discontinuities of the field lines.

The substantial advances in the measurement of solar vector magnetic fields in recent years have opened up a new possibility to observationally determine the topology skeleton in the Sun's active corona. In this paper, we used high-quality, high-cadence vector magnetograms and theoretical calculations to made a complete determination of the topology skeleton of magnetic fields for the solar active region (AR), NOAA 10720. The topology skeleton and its temporal evolution are explored, leading to an understanding of the explosive magnetic energy release in a major solar flare/CME event.

This paper is organized as followings: Section 2 is devoted to a description of observations of vector magnetic fields in AR 10720. Section 3 gives a brief introduction of the methods used in this work to determine the topology skeleton. Section 4 shows the main results of the study on the determined topology skeleton and its temporal evolution that led to the major flare and CME activity. Section 5 discusses possible uncertainty of the results. The conclusions are summarized in Section 6.

2 OBSERVATIONS OF VECTOR MAGNETIC FIELDS IN AR 10720

NOAA AR 10720 is a super AR which has produced the largest and hardest proton flux ($>$100 MeV) since 1989 and caused seriously disastrous conditions of space weather. It appeared on the solar disk as a simple beta magnetic sunspot on 2005 January 10 and ended as a large, magnetic complex sunspot region on January 22. It grew rapidly and showed impressive activity while it went across the solar disk. In the period January 14–21 it produced five X-class flares and 18 M-class flares. The vector magnetic fields were mapped by the Huairou Solar Observing Station (HSOS) vector-magnetograph (Ai & Hu 1986; Wang et al. 1996) from January 12 to 20, which provide clues for understanding the detailed magnetic evolution associated with the major flares. Big Bear Solar Observatory (BBSO) obtained vector magnetograms on January 14–15 with a high cadence of 1–2 minutes and a high resolution around 1 $''$–2$''$. The vector field evolution was thus traced round-the-clock from January 14 to 16.

The BBSO vector magnetograms were obtained by the Digital Vector Magnetograph (DVMG) system, and covered an area of about 300$''$ $\times$ 300$''$. The system consists of a 1/4 Å band pass birefringent filter, an SMD 1024 $\times$ 1024 12-bit CCD camera and polarization analyzer. Each data set consists of four images: a 6103 Å filtergram (Stokes-I), a line-of-sight magnetogram (Stokes-V) and the transverse magnetogram (Stokes-U and -Q). We rebinned the camera to the 512 $\times$ 512 mode to increase the sensitivity of the magnetograms.

The polarization analyzer includes two nematic liquid crystal variable retarders, whose retardance can be controlled with an applied voltage, to select a particular polarization state (6103 Å filtergram, Stokes V, Q, or U) by converting the desired input polarization set into an orthogonal set of linear polarizations.

A single ferroelectric liquid crystal, which is a fixed retarder whose rotation angle can be selected to be either 0 or 45 degree, acts as the system's fast modulator. This ferroelectric crystal, working with a fixed linear polarizer, is used to select one of the orthogonal linear polarization components. Light is then fed through the birefringent filter, and finally imaged onto the CCD camera. The exposure is typically 30 ms, and images are taken at a rate of approximately 12 frames s^{-1}.

A distinct characteristic of the evolution of the AR is the appearance of sheared emerging flux regions (EFRs) that carried current. They emerged successively and grew along the main magnetic neutral line of the AR. Figure 1 displays a time sequence of vector magnetograms obtained from the HSOS. These EFRs caused the AR to grow rapidly since January 13. On the figure four EFRs are marked by brackets. An important key characteristic of these EFRs is the appearance of a bundle of enhanced transverse fields that connected the growing magnetic fluxes of opposite polarity. The emergence of the four EFRs can be traced from January 13 until January 18. It is interesting that all these four EFRs were growing along the main magnetic neutral line, and separating in roughly opposite directions perpendicular to the main magnetic axis of the AR. It is noticed that the EFR marked close to the center of the magnetogram at 01:20 UT of January 15 showed twisting in the opposite sense, i.e., with opposite sign of magnetic shear or current helicity relative to the other EFRs. The co-existence of opposite helicity in new EFRs made the 3D magnetic configuration more complicated. Later from January 16 on, another new EFR appeared in the area of negative flux to the north of the magnetic neutral line (see the growing positive magnetic flux).

The effects of these EFRs are presented in several perspectives: (1) The magnetic neutral line was largely elongated. From Jan 13, 00:32 UT to Jan 15, 16:51 UT, the neutral line increased in length from 120 Mm to 260 Mm; (2) Interleafing of opposite polarities and multiple neutral lines appeared in the center of the AR; (3) Strong magnetic shear developed along the elongated neutral line in roughly the E-W direction. The net results of these EFRs appear to be equivalent to a widely spaced-out 'EFR', as indicated by the thick arrows in the magnetogram of Jan 16, 03:58 UT. Generally, the opposite polarities of newly emerged flux separated at a velocities of 0.5–0.7 km s^{-1} during the observed interval.

The central meridian passage of AR 10720 took place On January 15. An X-ray flare with significance X2.6 appeared at 22:25 UT in the AR. This flare is a good representative of flares associated with full-halo CMEs and serves as a typical active event worthy of careful exemplification. From 16:51 to 23:47 UT BBSO obtained 262 sets of high quality vector magnetograms with a 20 Gauss sensitivity in the line-of-sight magnetograms, and a 150 Gauss in the transverse magnetograms (Spirocks 2005). These observations fully confirmed the evolutionary characteristics of the vector magnetic fields in the AR revealed by the HSOS. In Figure 2, the evolution of the vector field over an interval of 7 hours is shown in details. The consistency in the flux distribution and field azimuth is impressive between the HSOS and BBSO magnetograms. The well-known 180 degree ambiguity in the observed field azimuth is resolved by the potential and constant-α force-free field assumptions. A few empirical corrections, based on the history of flux emergence and the continuity in the observed azimuth, were made after removing the ambiguity in the above objective ways.

There is no doubt that the topology skeleton in the magnetized plasma of the AR is determined by the magnetic field distribution and evolution in the photosphere. The BBSO vector magnetograms were obtained at much better seeing and with a cadence of 1–2 minutes. In addition, they covered the whole interval of the major flare/CME on January 15 from the pre-status to full-recovery phases. Thus, the BBSO magnetograms provide a rare opportunity to observationally determine the magnetic skeleton of a solar AR, and to identify the characteristics of its time evolution in the course of an explosive energy release in solar activity.

3 METHODS

We use the observed vector magnetograms of BBSO as the boundary condition, and, with the quasi-linear force-free code (Wang et al. 2001), we reconstruct the 3D magnetic fields of AR 10720. We can directly use the magnetograms which we selected very near to the center of the solar disk, ignoring solar rotation correction. Due to the influence of stray light, there exist areas of polarization saturation, which appeared as 'big holes' in the middle of the strong sunspots in the longitudinal magnetograms. The MDI longitudinal magnetogram at the nearest time is then used to fill these 'holes'.

The size of our extrapolation box is $250 \times 250 \times 150$ in units of bins. Each bin corresponds to $2.1''$. The observed magnetogram is embedded in the central 150×150, as shown in Figure 4.

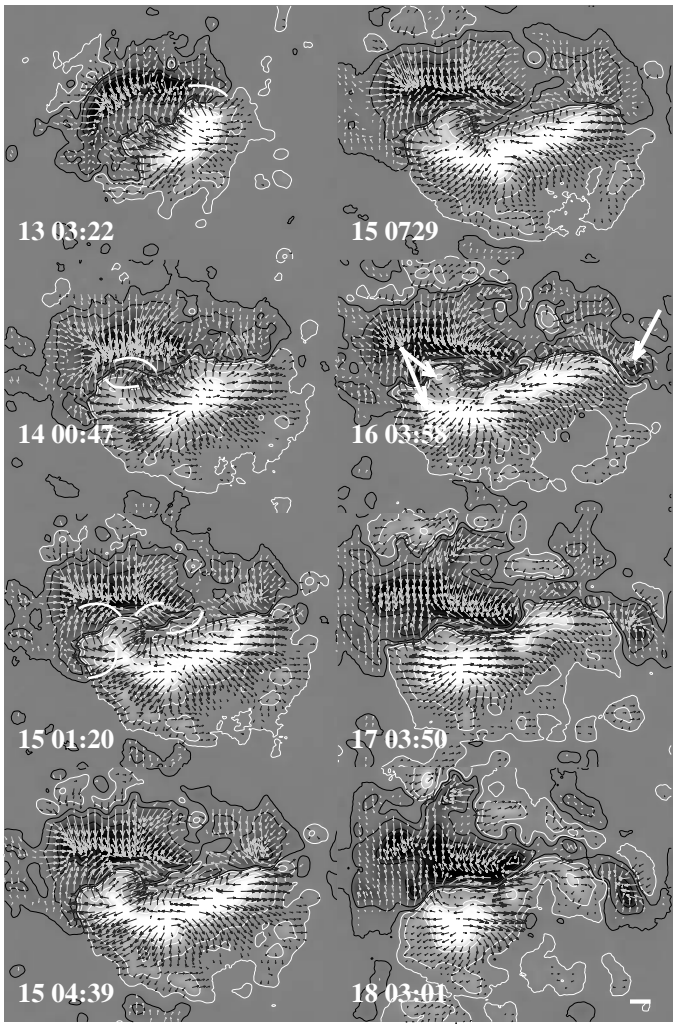

Fig. 1 Time sequence of the HSOS vector magnetograms. The line of sight component is shown by images scaled from –1500 to 1500 G and contours at levels of ± 50, 250, 500, 1000 and 1500 G. The transverse components are shown by short arrows with length proportional to the field strength and direction indicated by the arrow. Four key EFRs are marked in the magnetograms by brackets. Each EFR is characterized by a bundle of enhanced transverse fields and two growing footpoints of opposite polarity. In the Jan 16, 03:58 frame the three thick arrows indicate the concentrated magnetic flux of opposite polarity that came from the successive EFRs between January 13 and 16. The scale bar in the lower-bottom corner denotes 20.0 arcsec.

We searched for nulls in every cell of the box with the Poincaré index (Greene 1992; Zhao et al. 2005) after we obtained the 3D vector fields at each node in the AR. This method in 2D was used on vector magnetograms by Wang & Wang (1996). In 3D, we first obtain the magnetic vectors at the eight vertices of each cell, then we normalize these vectors and translate these images of vectors to the unit sphere. The cubic surface of each cell can naturally be separated into 12 triangles (see fig. 2 in Zhao et al. 2005), each triangle mapping a spherical triangle of the unit sphere. By integrating these 12 spherical triangles and dividing the integral by 4π, we effectively obtain the Poincaré index. A little different from the 2D case (Wang & Wang 1996), if a cell includes a null point, the index should be equal to 1 or –1, if not, then 0. Nulls with initial positions outside the middle 150 × 150 × 50 bins or lower than 1 grid were ignored, for then the extrapolation would not be reliable, or the foot points of the field lines through this region would go

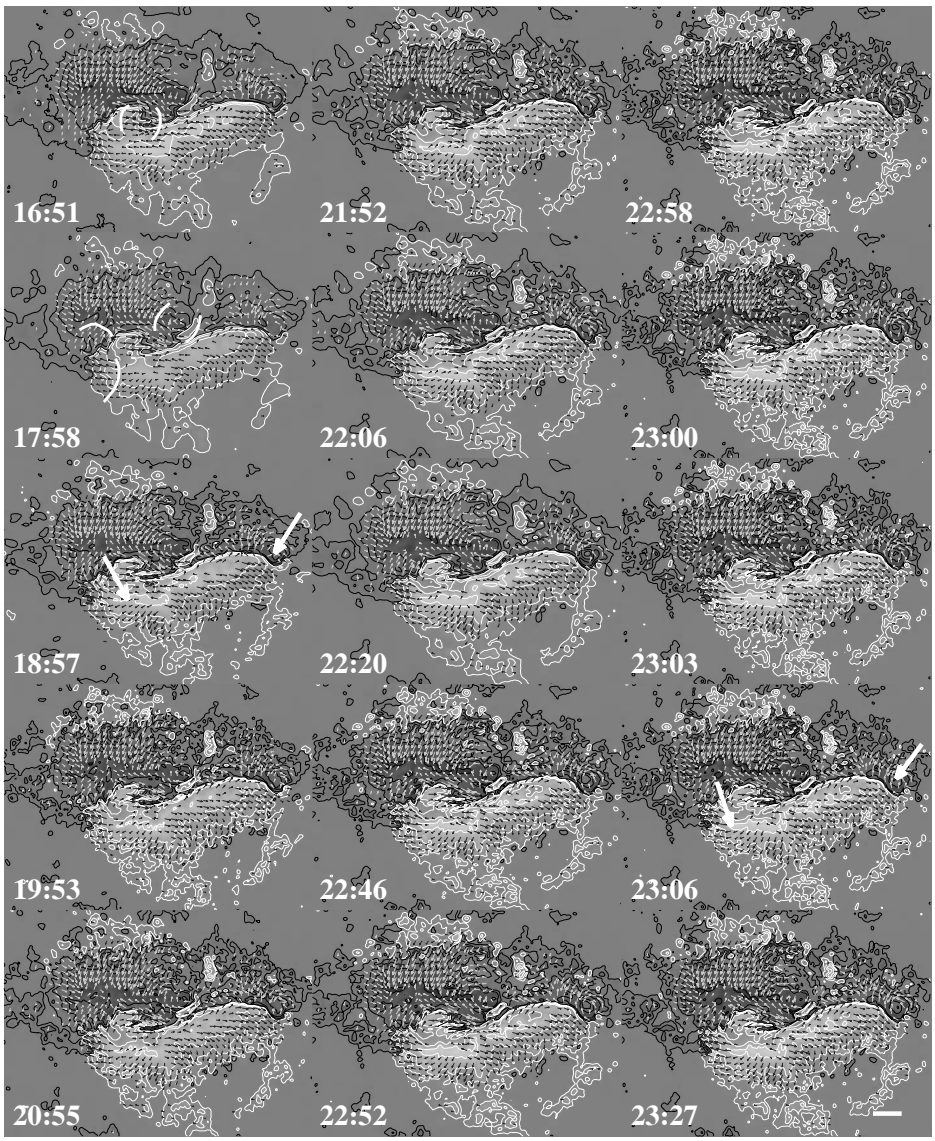

Fig. 2 Time sequence of the BBSO magnetograms shown in the same style as in Fig.1. Three continually growing EFRs are marked by brackets. Two sets of thick arrows indicate the concentrated magnetic flux of opposite polarity that came from the successive EFRs since Jan 13. Note, the opposite polarities of the equivalent EFR kept on growing and separating from each other. The scale bar denotes 25.0 arcsec.

beyond the observed region. We extended the scale of extrapolation when following the evolution of some particular nulls.

To draw out the magnetic skeleton above the active region, we calculate the field's Jacobian matrix $\delta \boldsymbol{B}$ at each identified null-point. The matrix $\delta \boldsymbol{B}$ has three eigenvalues and three eigenvectors, say, $\lambda 1$, $\lambda 2$, $\lambda 3$ and $\boldsymbol{v}1$, $\boldsymbol{v}2$, $\boldsymbol{v}3$. When the index is not equal to zero, the null would be a 3D isolated singular point. This means the null will not collapse into a 2D null (according to the definition of 3D isolated singular point), or the matrix $\delta \boldsymbol{B}$ is regular and none of the eigenvalue is zero. The trace of $\delta \boldsymbol{B}$ is equal to the sum of the three eigenvalues. On the other hand, the trace can be represented by $\nabla \cdot \boldsymbol{B}$ which is zero in a magnetic field. The three eigenvalues may be all real numbers or one is real number, the other two are conjugated complexes.

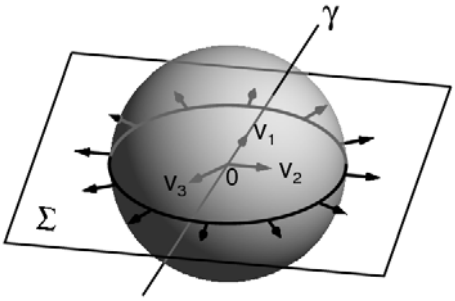

Fig. 3 An illustration of the structures near to a (B type) null. A unit sphere wraps round a cell containing the null. The γ line and the Σ surface of the null intersect cross the sphere at two points and in a circle, in the directions of the γ line and the Σ surface. These directions are determined by the three eigenvectors, $\boldsymbol{v}1$, $\boldsymbol{v}2$ and $\boldsymbol{v}3$, of the matrix $\delta\boldsymbol{B}$.

However, the real parts of them should be either (+ − −) or (− + +) (because the sum of the three real parts is zero). If they are all real numbers, the null is type A or type B; if two of them are complexes, the null is type As or type Bs (Cowley 1973; Lau & Finn 1990). One eigenvector ($\boldsymbol{v}1$ for example), corresponding to the only positive or negative eigenvalue, points out the direction of the γ line (or spine) and the other two ($\boldsymbol{v}2$ and $\boldsymbol{v}3$) determine the Σ surface (or fan) near the null-point (Fukao et al. 1975; Lau & Finn 1990). In practice, we select a small sphere (radius one grid unit) for each null that is big enough to include the cell. The spine and fan should intersect the sphere at two points and a circle respectively (Fig. 3). The vectors in the two points would be parallel to the spine eigenvector and the vectors on the circle would be parallel to the plane determined by the two fan eigenvectors. Thus, we can know which point on the sphere belongs to the intersection of the line of spine or fan by check whether the directions of the vectors on the sphere are parallel to the directions of spine or fan. We draw lines of the fan $l(x)$ starting from the sphere along the circle, where x belongs to the circle, if an infinitely small distance ϵ in the point x makes the other endpoints of $l(x-\epsilon)$ and $l(x+\epsilon)$ to deviate sharply from each other, then there must be a separator line $ls(x)$ starting from x. When the two endpoints of a separator are both null, the separator is called a null-null line. Finally, we obtain the magnetic skeleton composed of nulls, spines fans and separators.

4 TOPOLOGY SKELETON OF AR 10720

Using the observed vector magnetograms as boundary conditions, we first reconstruct the 3D magnetic fields in the AR's atmosphere with a quasi-linear force-free code (Wang et al. 2001); then we identify the 3D magnetic nulls by a differential geometry approach (Greene 1992; Zhao et al. 2005) in the extrapolated vector fields; finally we determine the magnetic skeleton by connecting the nulls, spines, fans and separators. We compare the skeletons with flare ribbons and EIT light structures, also we examine the skeleton evolution from the derived time-sequence of topologies.

4.1 Determined Topology Skeleton

The determined skeleton at 21:25 UT of January 15 basically consists of six nulls (see Fig. 4). Each null and its associated γ-line (spine) and Σ-surface (fan) are referred to as a topology, and numbered as Topologies I, II, ..., VI, respectively. Their locations, eigenvalues, and divergence of magnetic vector in term of observational errors are listed in Table 1. A majority of the magnetic lines of force (see the lower panel of Fig. 4) anchored in the photosphere are bound by a combination of fans and spines of the Topologies I, II, III, and V, and forms the magnetized atmosphere of the AR. Topology IV is embedded in the middle of the atmosphere.

Of the six nulls, Null IV is of type As, i.e., a spiralling-in null. It is located at an altitude of 47 Mm. For the first time we have identified a spiral null of an AR in the Sun's corona, based on observations. The spine of the As null lies above the whole length of the magnetic neutral line, along which the 'sheared

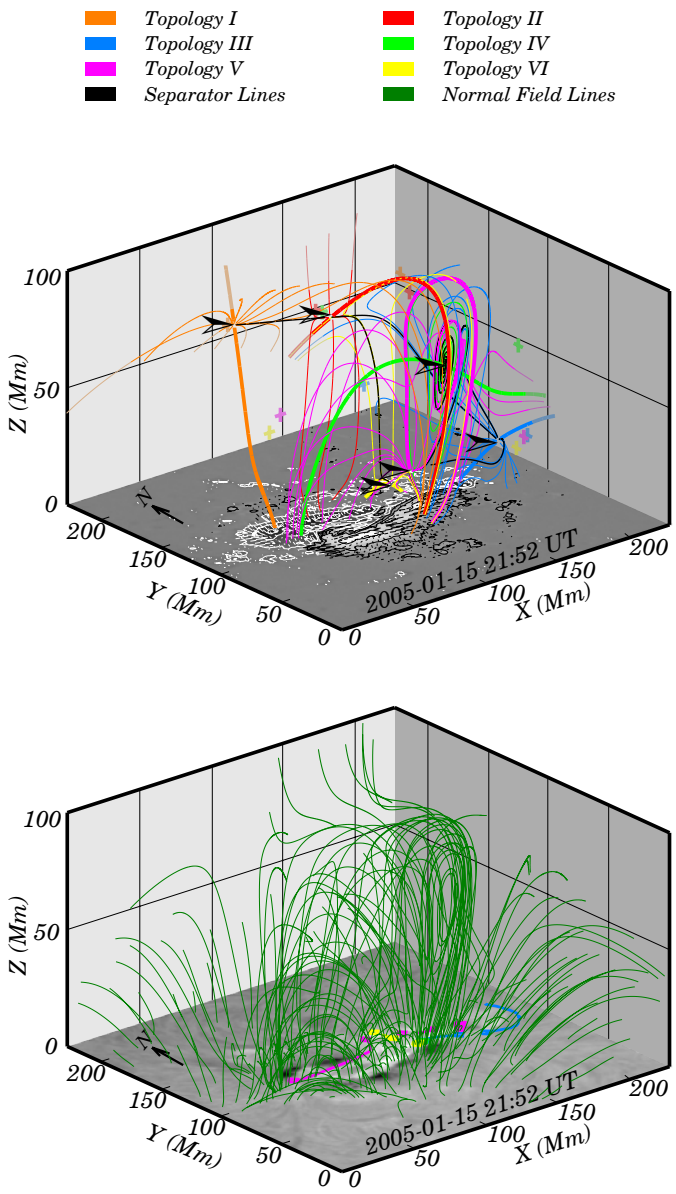

Fig. 4 3D magnetic structures and determined topology skeleton of AR10720. The magnetic lines of force extrapolated by a quasi-linear force-free code based on the observed BBSO vector magnetogram at 21:52 UT on January 15, 2005 are shown in the lower panel; while the magnetic skeleton determined from the extrapolated 3D fields is shown in the upper one. The vector magnetogram is displayed as the background in the upper one, in which the line-of-sight flux density is shown by grey map with contours of 200, 700, 1200 Gauss and bright (dark) color for positive (negative) flux; the transverse magnetogram is shown by short arrows with length representing the field strength. A null and its spine and fan are referred to as a topology, and the topologies are numbered from 'I' to 'VI'. The positions of the nulls are indicated by arrows while their projections in the two vertical planes are marked by the symbols '+'. Different topologies are drawn in distinct colors. Thick lines are spines while thin lines are magnetic lines on the fans. A BBSO Hα filtergram is shown as the background of lower panel, in which the intersections of the fans with the chromosphere are drawn to show their correlation with the flare ribbons.

Table 1 Parameters of nulls at 21:52 UT. We use the coordinates of Fig. 1 to mark the nulls' positions. ΔB=100 G (0.01 T) and $L = 1$ unit grid (1.523 Mm). $|\langle \Delta B \rangle / \langle L \rangle|$ denotes the average error in the derivatives of the observed magnetic field.

No	Type	Position (Mm)	Eigenvalues (10^{-10} T m^{-1})	$\frac{\lvert \nabla \bullet B \rvert}{\lvert \langle B \rangle / \langle L \rangle \rvert}$
I	A	(111,222,55)	0.967, –0.115, –0.194	0.010
II	B	(172,215,49)	–0.167, 0.080, 0.592	0.008
III	A	(207,117,11)	1.847, –0.523, –0.814	0.008
IV	As	(177,125,47)	0.308, –0.038$\pm$0.735i	0.004
V	B	(148,120,9)	–3.120, 1.079, 4.405	0.036
VI	A	(140,126,3)	4.795, –2.620, –4.738	0.039

EFRs' emerged (see Figs. 1 and 2). Around the spine of the As null the magnetic lines of force twisted, forming a magnetic wreath shaped like a trumpet shell, i.e., a complicated flux rope structure. This structure obviously can be a kind of physical flux rope, a concept commonly used, but a rope structure may not have an As or Bs null in its center. The Fan V and a part of the Fan III join to the twisted lines of force. In fact, the rotated lines of force which consist of the rope-like structure at the boundary with Fan III, Fan IV and Fan V. The electric current density flowing along the spine is as high as 3×10^{-4} A m^{-2} at such an altitude in the corona. It is, at least, two times higher than that in surroundings, indicating a concentration of free magnetic energy. The currents also flowed in the fan surface, which resulted in a tilt angle of 75 degrees between the spine and fan.

The main rope-like structure is composed of Topology IV and Topology V, derived from Null IV and Null V, respectively. As we know, the complicated structure centered with a null-null pair consisting of one or two spiral nulls is only described by numerical simulations based on plasma kinetic approaches (Büchner 1999; Cai et al. 2006). To display more clearly the structure of the As-B null pair, we show a simplified idealized cartoon in Figure 5. Here Σ_{A_s} intersects Σ_B in the A_s-B null-null line, the separator, and Σ_{A_s}, Σ_B are semi-infinite sheets bounded by γ_B, γ_{A_s}, respectively. The field lines on Σ_{A_s} twisted into the A_s null, and Σ_B rolls over onto γ_{A_s} (note that part of the field lines on Σ_B asymptotically approaches, but does not touch γ_{A_s}). The field lines on Σ_B which asymptotically approach the γ_{A_s} and the field lines on Σ_{A_s} form a rope-like structure. We should point out that in Figure 4 the Fan IV, a Σ_{A_s} surface, is not a semi-infinite sheet because it is bounded not only by Spine V, a γ_B line, but also by the photosphere.

The six nulls are connected by a net of null-null lines, the so-called separators, on which the frozen-in magnetized plasmas of four individual topologies are in close contact and interact with one another. The adjacent null pairs in the separators are all of A-B or As-B type. These fans and their intersections, the separators, separate the magnetized atmosphere into different domains in which the lines of force have the same connectivity. The net of separators bridging distinct topologies goes through the magnetized atmosphere. This fact hints at the characteristic of 3D magnetic reconnection in the AR. As reconnection could take place successively or simultaneously along the whole separator net, the magnetic energy release during the reconnection in the AR should be global, fast and explosive in nature (Priest et al. 1997; Priest & Forbes 2000; Parnell 2007).

4.2 Relations with Flare Ribbons and Brightening EUV Loops

It is interesting that the cross-sections of spans of the lower Topologies III, V, and VI coincided with the main parts of the flare ribbons (see the lower panel of Fig. 4) as described by many authors previously (see Démoulin et al. 1997). The S-W portion of the flare ribbons apparently avoided all the topology structures, but was, in fact, clearly connected to the fans of Null V by a set of magnetic arcades straddling the magnetic neutral line.

Such complicated rope structures organized by a spiral null were never anticipated until we drew out the topology skeleton. The Fans IV and V intersect at the As-B null-null line, the separator, and they are bounded asymptotically by Spines V and IV, respectively. The field lines on Fan IV twist into Null IV, the As type null, and Fan V rolls over onto Spine IV. The field lines on Fan V that asymptotically approach Spine IV, the field lines on Fan VI and a fraction of those on Fan III compose the frame of the magnetic

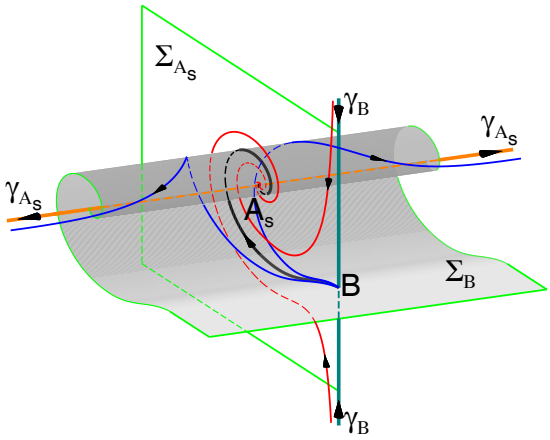

Fig. 5 A cartoon to sketch in simplified the topology structure of the A_s-B null-null pair. Orange and celadon lines are γ_{A_s} and γ_B lines respectively. Red and blue lines represent fields lines on Σ_{A_s} and Σ_B. The black line marking the intersection of Σ_{A_s} and Σ_B is the A_s-B null-null line. Note, the magnetic lines of force on the two sides of Σ_{A_s} twist in opposite sense.

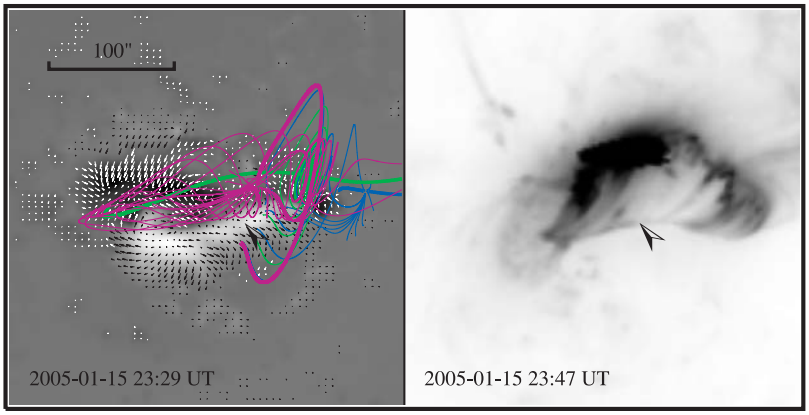

Fig. 6 Comparison of the magnetic wreath associated with the spiral null (left panel) and the EUV brightening structure in the late phase of the X2.6 flare (right panel). Left: The topology skeleton is superposed above a BBSO vector magnetogram at 23:29 UT. Right: The general appearance of the EUV brightening structures is shown in reversed color code (brightest structures are coded darkest). The EUV structures resemble the topology skeleton, particularly the low sharp boundary seems to coincide with the low boundary of the wreathed Σ surfaces of Nulls III and V (indicated by the arrows).

wreath. It is remarkable that the magnetic lines of force on the two sides of Fan IV twist in opposite senses i.e., the magnetic helicity in the rope-like structure does not keep the same sign. Although our analysis here did not reveal the details of the associated 3D reconnection, we noticed a close similarity between the 'magnetic wreath' and the EUV rope-like structures that brightened in the course of the flare/CME (see Fig. 6). The EUV brightening took place in a twisting structure similar to the magnetic lines of force in the magnetic wreath, i.e., the general shape and sharp boundaries of the EUV structure well resembled the magnetic wreath. This implies a close correlation between the energy release and topology structure.

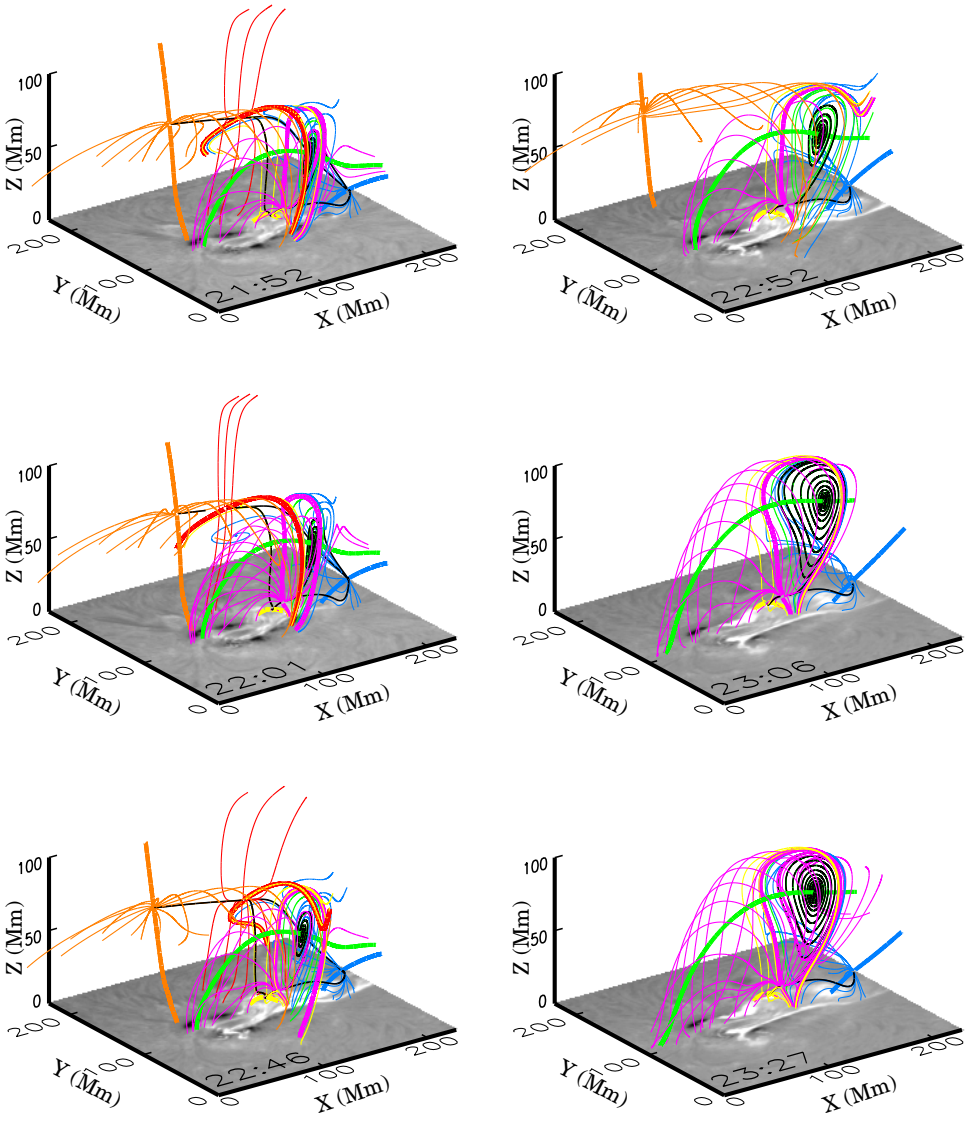

Fig. 7 Skeleton evolution in the interval from the pre-state to the recovery phase of the flare/CME. Null II and its topology disappeared between 22:46 and 22:52 UT, during which the CME started from the solar disk, while Null I and its topology disappeared between 23:03 and 23:06 UT at the maximum phase of the flare. Same drawing style as in Fig. 1. The rising of Null IV and the magnetic wreath are clearly shown in the time-sequence.

4.3 Evolution of Skeleton

Based on the observed time sequence of vector magnetograms, we further deduced the evolution of the topology skeleton from 21:52 to 23:47 UT (see Fig. 7), covering the interval from the pre-status to recover-phase of the flare/CME. In this time, the topology skeleton showed obvious evolution, which could be categorized into slowly systematic evolutions and explosive eruptions. One of the key systematic evolutions is the rising of the spiral null together with its spine. The spiral null moved up more than 26 Mm during the studied interval. At the same time, the magnetic wreath grew in size. Accordingly, there is also an expansion

of Topology I. In the expansion, Null I moved northward more than 50 Mm between 21:52 and 22:52 UT. This dramatic evolution is likely a response to the rapid growth of the 'sheared EFRs'. During this interval the apparent speed of separation of the opposite polarity flux of the EFRs was about 1.0 km s^{-1}. The fast and continuous separation of opposite polarities of the new emerging flux can be seen clearly from the S-W movement of the negative flux patch (already grown to a sunspot) indicated by a thick arrow in Figure 2.

In the course of the systematic evolution two topology eruptions took place in association with the flare-CME development. Null II and its topology erupted right before the flare and shortly after the initiation of the halo CME at 22:36 UT, which passed into LASCO C2 field of view at 23:06 UT with a speed of more than 2800 km s^{-1}. The second topology eruption appeared at the maximum phase of the flare and manifested itself by the disappearance of Null I and its topology. The separators connecting the Nulls I and II disappeared in the two topology eruptions, which is indicative of vigorous 3D magnetic reconnection along the null-null lines in the flare/CME event. However, we may not exclude the possibility that the two 'disappeared' topologies might have simply moved outside the domain of calculation. To test this possibility, we have extended our calculations to more than 200 Mm above the photosphere, but found no hints of their existence in the higher corona. During the skeleton evolution, the three lower nulls, Nulls III, V and VI, and their topologies remained, keeping unchanged their spatial relations with the flare ribbons.

5 DISCUSSION

There may appear some uncertainties in the determination of magnetic skeletons, coming mainly from the 3D reconstruction of magnetic fields. We have examined the reliability of the approaches in this work by artificially introducing random noises in the observed magnetograms, and found that the basic skeletons that we determined are reproducible.

It is well-known that with the same boundary condition different algebra and codes would give different force-free solutions, i.e., the extrapolation of force-free fields from observations is not unique (Seehafer 1978). We have tested the robustness of our findings by using different force-free codes. First, the skeleton which we determined could not be well reproduced using the potential and linear force-free field extrapolation models and methods (Alissandrakis 1981; Seehafer 1978; Chiu & Hilton 1977). The potential and exactly constant-α force-free extrapolations were important in finding spiral nulls. The reason is that opposite helicity signs are maintained in the magnetic structures when there is a spiral null and the co-existence of opposite sign helicity, hence an α value is not allowed in the potential or linear force-free models.

These new skeletons reconstructed by the other extrapolation codes have a poor relation with the flare ribbons and it emerged that the potential and exactly constant-α force-free extrapolations were important in finding spiral nulls, and that a right transverse field is necessary for the reconstruction based on a complicated vector magnetogram with strong shearing.

For a severely twisted or sheared magnetic topology, the codes based on boundary element method (BEM) developed by Wang et al. (2001) and Yan & Sakurai (2000) may prove advantageous. In a comparison based on an analytical model (Low & Lou 1990), the BEM (Liu et al. 2002) performed better than the potential and constant α methods and produced less disparity nearer the center of the extrapolation box (Schrijver et al. 2006).

We have tried to use other non-linear force-free models (Wheatland et al. 2000; Wheatland 2006, 2007; Song et al. 2006) to examine if the current results can be repeated by other code independently. More work still need to be done before drawing definitive conclusions. The complicated topology skeleton determined in this study has not been reproduced by other potential and linear force-free codes so far, the reality of the determined skeleton can only be hinted by comparison with the observations of brightness structures in Hα, EUV, and X-ray wavebands. As shown by Figures 4, 6 and 7, the Hα flare ribbons are closely associated with the lower nulls and their topologies, while the higher nulls (including the spiral null) and their topologies are more closely correlated with the CME onset. Because our determined topology skeleton does match some of the activity structures in both spatial and temporal domains, we believe that our determination indicates, at least, some of the peculiarities of the real 3D topology.

More active regions are under consideration and a few different force-free codes are considered in our future efforts to observationally determine the topology skeleton of magnetic fields. For the 3D vector field measurements, either by *in situ* or remote-sensing, our method to determine the 3D nulls can be useful and robust.

6 CONCLUSIONS

Based on the time sequence of observed vector magnetograms of high resolution and sensitivity, we have determined the 3D magnetic skeleton and its evolution in a solar AR. We have identified, for the first time, the spiral magnetic null in the solar corona. Extremely complicated rope structures, and the magnetic wreath, associated with the spiral null appear to be the central ingredient of the magnetic skeleton. The determined skeleton has close tempo-spatial associations with solar explosive activity. The skeleton evolves in response to the evolving vector field in the solar photosphere. We have clearly uncovered two topology eruptions in the course of the flare/CME. The complexity of the observed magnetic skeleton and its evolution in solar active atmosphere we found have not been previously reported.

Although spiral nulls are predicted in some theoretical studies (Lau & Finn 1990; Parnell et al. 1996), they have never been discovered in solar observations. On the other hand, their appearance and role in 3D magnetic reconnection have been clearly revealed by numerical simulations based on plasma kinetic approaches (Büchner 1999; Cai et al. 2006). Our observations fully support the theoretical predictions and numerical simulations. For many years solar astronomers have hypothesized common existence of flux ropes in Sun's corona. The flux rope concept becomes a central element in the modeling of the CME, but observational identification was not available previously. Different authors used the same scientific term, 'flux rope' to refer to different physical entities in observations (Hudson & Cliver 2001). Here we propose that the magnetic topology of a spiral null in the corona, e.g., the magnetic wreath, serves, at least, one type of the real flux ropes. Flux ropes are likely to have spiral nulls inside in reality. Their magnetic structures appear to be more complicated than have been thought. Within a flux rope magnetic helicity of opposite signs can be kept in association with topology peculiarities. The magnetic reconnection between opposite helicity flux may result in explosive release of more free magnetic energy (Wang et al. 2004).

Acknowledgements This work was supported by the National Basic Research Program of China (2006CB806303) and the National Natural Science Foundations of China (Grants 10573025 and 40674081). Many thanks go to H. N. Wang, E. R. Priest, M. S. Wheatland and M. T. Song for kind assistance.

References

Ai G., Hu Y., 1986, Publ. Beijing Astron. Obs., 8, 1
Alissandrakis C. E., 1981, A&A, 100, 197
Aulanier G., DeLuca E. E., Antiochos S. K. et al., 2000, ApJ, 540, 1126
Brown D. S., Priest E. R., 2001, A&A, 367, 339
Büchner J., 1999, Astrophys. and Space Sci., 264, 25
Bungey T. N., Titov V. S., Priest E. R., 1996, A&A, 308, 223
Cai D., Nishikawa K., Lembege B., 2006, Plasma Phys. Control. Fusion, 48, B123
Chiu Y. T., Hilton H. H., 1977, ApJ, 212, 873
Cowley S. W. H., 1973, Radio Sci., 8, 903
Démoulin P., Henoux J. C., Mandrini C. H., 1992, Solar Phys., 139, 105
Démoulin P., Henoux J. C., Priest E. R., Mandrini C. H., 1996, A&A, 308, 643
Démoulin P., Bagalá L. G., Mandrini C. H. et al., 1997, A&A, 325, 305
Filippov B., 1999, Solar Phys., 185, 297
Fletcher L. et al., 2001, ApJ, 554, 451
Fukao S., Masayuki U., Takao T., 1975, Rep. Ionos. Space Res. Jpn., 29, 133
Giowanelli R. G., 1946, Nature, 158, 81
Gorbachev V. S., Somov B. V., 1988, Solar Phys., 117, 77
Greene J. M., 1992, J. Comp. Phys., 98, 194
Hudson H. S., Cliver E. W., 2001, J. Geophys. Res., 106, 25199
Lau Y. T., 1993, Solar Phys., 148, 301
Lau Y. T., Finn J. M., 1990, ApJ, 350, 672
Li H., Schmieder B., Aulanier G., Berlicki A., 2006, Solar Phys., 237, 85
Liu Y., Zhao X. P., Hoeksema J. T. et al., 2002, Solar Phys., 206, 333
Longcope D. W., 2005, Living Rev. Solar Phys., 2, 7
Longcope D. W., Klapper I., 2002, ApJ, 579, 468

Low B. C., 1987, ApJ, 323, 358
Low B. C., Lou Y. Q., 1990, ApJ, 352, 343
Low B. C., Wolfson R., 1988, ApJ, 324, 574
Maia D. et al., 2003, A&A, 405, 313
Parnell C. E., 2007, Mem. S.A.It., 78, 229
Parnell C. E., Smith J. M., Neukirch T., Priest E. R., 1996,J. Plasmas Phys., 3, 759
Priest E. R., Bungey T. N., Titov V. S., 1997, Geophys. Astrophys. Fluid Dyn., 84, 127
Priest E. R., Démoulin P., 1995, J. Geophys. Res., 100, 23,443
Priest E., Forbes T., 2000, Magnetic reconnection: MHD theory and applications, Cambridge: Cambridge Univ. Press
Schrijver C. J., Derosa M. L., Metcalf T. R. et al., 2006, Solar Phys., 235, 161
Seehafer N., 1978, Solar Phys., 58, 215
Seehafer N., 1986, Solar Phys., 105, 223
Spirocks T., 2005, thesis, New Jersey Institute of Technology
Song M. T., Fang C., Tang Y. H. et al., 2006, ApJ, 649,1084
Sweet P. A., 1958, IAU symposium, 6, 123
Titov V. S., Hornig G., Démoulin P., 2002, J. Geophys. Res., 107, 1164
Titov V. S., Priest E. R., Démoulin P., 1993, A&A, 276, 564
Wang H. N., Yan Y. H., Sakurai T., 2001, Solar Phys., 201, 323
Wang H. N., Wnag J. X., 1996, A&A, 313, 285
Wang J. X., Shi Z. X., Wang H. N., Lü Y. P., 1996, ApJ, 456, 861
Wang J. X., Zhou G. P., Zhang J., 2004, ApJ, 615, 1021
Wheatland M. S., Sturrock P. A., Roumeliotis G., 2000, ApJ, 540, 1150
Wheatland M. S., 2006, Solar Phys., 238, 29
Wheatland M. S., 2007, Solar Phys., submitted
Xiao C. J. et al., 2006, Nature Phys., 2, 478, DOI: 10.1038/nphys342
Yan Y. H., Sakurai T., 2000, Solar Phys., 195, 89
Zhao H., Wang J. X., Zhang J., Xiao C. J., 2005, Chin. J. Astron. Astrophys. (ChJAA), 5, 443